



Peeling from elastomeric layers: Does material compressibility matter?

Hang Li, Zhaohe Dai^{*,*}

Department of Mechanics and Engineering Science, State Key Laboratory for Turbulence and Complex Systems, College of Engineering, Peking University, Beijing 100871, China

ARTICLE INFO

Keywords:

Elastomeric layers
Peeling
Elastic foundations
Delamination
Compressibility
Adhesives

ABSTRACT

Elastomeric adhesives are widely used in various engineering systems, where the adhesive layer typically resides between two flexible or rigid adherents. In this context, the mechanics “ingredients” of the confined adhesive layer—such as its thickness, elastic modulus, and Poisson’s ratio—play a role as critical as surface chemistry in the adhesion performance. This has been demonstrated recently in a canonical configuration: lifting or peeling a flexible plate from a confined adhesive layer. While this configuration has been extensively discussed under the assumptions of perfect material compressibility or incompressibility, adhesives such as elastomeric layers are rarely perfectly compressible or incompressible in practice. Herein, we investigate the peeling of plates from adhesive layers with arbitrary material compressibility. We show that neither zero-pressure nor the zero-pressure-gradient conditions at the delamination front used previously are strictly necessary, though the former provides a good approximation in planar cases. We then combine analytical solutions, finite element analysis, and desktop experiments to show that even elastomeric adhesive layers are approximately compressible due to their geometrical slenderness. Consequently, the distinction between the zero-pressure and zero-pressure-gradient assumptions is negligible in practical applications as long as the energy release rate is properly considered.

1. Introduction

Adhesive bonding is essential in a wide range of modern applications, including microelectromechanical systems (MEMS) [1,2], actuators [3], coatings [4,5], and biomedical devices [6–9]. In a typical bonding process, adhesives initially behave as viscous or visco-plastic fluids that can fill the gap between two rigid or flexible adherents. Upon solidification, a thin adhesive layer forms, bonding the adherents [10]. In such configurations, the mechanical properties of the adhesive layer are just as critical as its chemical composition in determining bonding performance [11,12]. For example, it has been shown that the critical force required to peel a flexible plate from an elastomer layer bonded to a rigid base depends not only on the intrinsic interfacial toughness but also on the adhesive’s thickness, Young’s modulus, and Poisson’s ratio [13–18]. Therefore, an important question in adhesive bonding systems is how the thin adhesive layer deforms and cracks under mechanical loads.

A commonly used model for the deformation of thin elastic layers is the so-called Winkler’s mattress model, or elastic foundation model [19], in which the vertical deformation of the layer surface w at a position $\mathbf{x} = (x, y)$ is linearly proportional to the local normal traction

$$p(\mathbf{x}), \text{ i.e., } w(\mathbf{x}) = \frac{p(\mathbf{x})}{k_W}, \quad (1.1)$$

where k_W is the Winkler stiffness. Skotheim and Mahadevan [20] used an analogy to hydrodynamic lubrication theory to show that the Winkler stiffness can be expressed as

$$k_W = \frac{2(1-\nu)G}{1-2\nu} \frac{1}{d}, \quad (1.2)$$

where ν , G , and d represent the Poisson’s ratio, shear modulus, and thickness of the layer, respectively. In this model, the elastic layer is represented as an array of disconnected elastic springs, and the square-root singularity in classical linear elastic fracture mechanics is absent. Nonetheless, variational analysis and the J -integral approach have been used to evaluate the corresponding energy release rate for Winkler elastic foundations:

$$\mathcal{G} = \frac{p^2}{2k_W} = \frac{1}{2}pw = \frac{1}{2}k_W w^2. \quad (1.3)$$

at the contact edge or delamination front [21–25]. Delamination occurs when $\mathcal{G} = \gamma$, where γ is the effective interface toughness between the layer and the adherent.

* Corresponding author.

E-mail address: daizh@pku.edu.cn (Z. Dai).

Markedly, the Winkler elastic foundation becomes rigid for incompressible adhesives since $k_W \rightarrow \infty$ as $\nu \rightarrow 1/2$, which is unphysical. In practice, an incompressible layer can deform through shear deformation, which is not accounted for by the Winkler model [26,27]. Dillard [26] demonstrated that the vertical deformation of perfectly incompressible thin layers depends on the second derivative of the pressure, which can be expressed as

$$w(x) = -\frac{1}{k_1} \nabla^2 p(x), \quad (1.4)$$

which have also been extended for two-dimensional (2D) configurations in Refs. [14,27], where $\nabla^2 = \partial^2/\partial x^2 + \partial^2/\partial y^2$ is the 2D Laplacian. The incompressible modulus k_1 depends on the boundary conditions at the layer's surface. For instance, $k_1 = 12G/d^3$ for zero surface shear displacement [26,28] and $k_1 = 3G/d^3$ for zero surface shear traction [27], similar to the prefactor in lubrication theory [29,30].

The incompressible foundation model has been widely used to analyze phenomena such as soft lubrication, indentation, and plate buckling instabilities on thin elastomeric layers [19,27,31,32]. However, its application to adhesive bonding problems is challenged by the fact that the Laplacian of pressure demands higher-order continuity or matching conditions at the delamination front. To address this, one approach, used by Ghatak et al. [14] and Plaut and Dillard [33], assumes

$$\frac{dp}{dx} = 0 \quad (1.5)$$

at the delamination front and solves the problem within the framework of Griffith fracture or Johnson–Kendall–Roberts (JKR) adhesion theory. Another approach instead imposes

$$p = 0 \quad (1.6)$$

at the delamination front and incorporates a non-zero pressure gradient to characterize the effect of adhesive forces [15,23,34–36]. Both approaches exhibit certain agreement with experiments and cohesive-zone modeling simulations [14,35,37]. From the perspective of boundary layer analysis, however, the stress state near the delamination front is inherently singular and three-dimensional, making both approaches approximate at best [38,39]. This raises the critical question of which approach provides the better approximation for a given setup.

While the use of zero-pressure or zero-pressure-gradient conditions may only result in quantitative differences in modeling the thin-layer debonding, qualitative discrepancies arise from the non-ideal compressibility of real adhesives. For example, the Poisson's ratio of elastomeric adhesives is rarely exactly $1/2$ but typically falls within the range $0.45 \lesssim \nu \lesssim 0.5$ [40], meaning that neither the perfectly compressible nor the perfectly incompressible foundation model is fully applicable [27,41]. This issue is further exacerbated by the thin geometry of the adhesive layer, which causes the effective material compressibility influenced by both the Poisson's ratio and the layer's slenderness [27,42–44]. Consequently, rather than relying on idealized compressible or incompressible models, it is more appropriate to address adhesive bonding problems using a framework that accounts for arbitrary compressibility. Such an approach would also provide a way to resolve current theoretical ambiguities regarding the zero-pressure or zero-pressure-gradient conditions.

To address the puzzle of “zero pressure” versus “zero pressure gradient” as well as “compressible” versus “incompressible”, we investigate the canonical configuration: the peeling of a flexible plate from an adhesive layer with *arbitrary* compressibility. Specifically, we will adopt a high-order foundation model and derive a generalized delamination condition using a J -integral approach. The results demonstrate that neither the zero-pressure nor the zero-pressure-gradient assumptions are strictly necessary. Furthermore, we will show that even elastomeric adhesive layers are likely compressible in practice, suggesting that the distinction between the zero-pressure and zero-pressure-gradient assumptions is negligible, as long as the energy release rate is properly

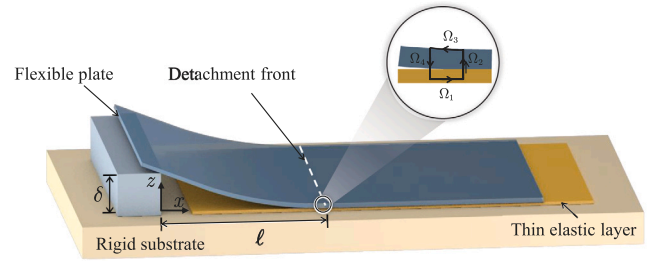


Fig. 1. Schematic illustration and notation for peeling a flexible plate from a thin elastic layer. The plate of bending stiffness B adheres to a thin elastic layer of shear modulus G , Poisson ratio ν , and thickness d . The left end of the plate is lifted with a vertical displacement δ and the interface is then delaminated with a length ℓ . The zoom-in view illustrates the paths for J -integral calculation around the delamination front.

accounted for. The remainder of the paper is organized as follows: In Section 2, we introduce the model for thin adhesive layers with arbitrary allowable Poisson's ratio in a planar setting and discuss the corresponding delamination conditions. In Section 3, we compare the results obtained using zero-pressure and zero-pressure-gradient conditions. The effective compressibility is also discussed through a combination of analytical solutions, cohesive zone modeling, and experiments. Finally, we summarize the key findings and implications of this work in Section 4.

2. The model

2.1. Problem description

Inspired by the experimental setup in Ref. [14], we consider a flexible plate adhered to a thin elastic layer, which is bonded to a rigid substrate (see Fig. 1). The primary focus is on the peeling force F required to induce a vertical displacement δ at the left end of the plate ($x = 0$) and the corresponding delamination length ℓ . To characterize the mechanical response of a thin layer with arbitrary Poisson's ratio, we employ the “combined foundation” model recently developed by Chandler and Vella [27] through a perturbation analysis, where the thinness of the layer is treated as a small parameter. Specifically, the displacement $w_s(x)$ of the thin layer is given by:

$$w_s(x) = \frac{1}{k_W} p(x) - \frac{1}{k_1} \nabla^2 p(x), \quad (2.1)$$

where the first term on the right-hand side represents the Winkler-type volume-changing deformation of the thin elastic substrate, and the second term accounts for the shape-changing (shear) deformation [27]. Assuming a no-slip interface between the plate and the thin layer, the foundation stiffness is given by:

$$k_W = \frac{2(1-\nu)}{1-2\nu} \frac{G}{d} \quad \text{and} \quad k_1 = \frac{3(1-\nu)^2}{(3/4-\nu)(\nu-1/4)} \frac{G}{d^3}, \quad (2.2)$$

where G is the shear modulus, d is the thickness, and ν is the Poisson's ratio of the substrate [27]. Clearly, this combined foundation model reduces to the perfectly incompressible model in Eq. (1.4) when $\nu \rightarrow 1/2$ [26]; It also reduces to the perfectly compressible model in Eq. (1.2) when the slenderness is sufficiently large and the Poisson's ratio is not too close to $1/2$. Note that for transversely isotropic thin layers, the asymptotic analysis incorporating higher-order terms leads to a foundation model of the same form as in Eq. (2.1) [45,46].

We assume that the plane-strain deformations $w(x)$ of the thin flexible plate, with bending stiffness B , are governed by the Kirchhoff–Love plate theory [47]:

$$Bw'''' + p = 0, \quad (2.3)$$

where $w' = dw/dx$ and p represent the interaction force between the plate and the thin layer. As illustrated in Fig. 1, we have $p = 0$ in the delamination region ($0 < x < \ell$) and $w = w_s$ in the contact region ($x > \ell$). Combining Eqs. (2.1) and (2.3) yields a single governing equation for the deflection of the plate:

$$k_1 B w'''' + k_w (k_1 w - B w''''') \mathcal{H}(x - \ell) = 0, \quad (2.4)$$

for $x > 0$, where \mathcal{H} is the Heaviside step function. This formulation differs from prior studies involving plates on perfectly compressible layers [21,23–25] and perfectly incompressible layers [14,24,33,35,39].

Eleven boundary/matching conditions are required to solve this multipoint boundary value problem (10 for the ordinary differential equations and 1 for the unknown delamination length ℓ). For the setup shown in Fig. 1, the natural boundary conditions are:

$$w(0) = \delta, \quad w''(0) = 0, \quad w(\infty) = 0, \quad w'(\infty) = 0, \quad w''(\infty) = 0, \quad (2.5)$$

and the continuity of deflection, slope, curvature, and shear force requires:

$$\llbracket w(\ell) \rrbracket = \llbracket w'(\ell) \rrbracket = \llbracket w''(\ell) \rrbracket = \llbracket w'''(\ell) \rrbracket = 0, \quad (2.6)$$

where $\llbracket f(\ell) \rrbracket = f(\ell^+) - f(\ell^-)$ denotes the jump across the delamination front at $x = \ell$. Such high-order continuities differ from the peeling of a plate from a rigid substrate, where the curvature exhibits a jump across the delamination front [48–52].

To determine the condition for the delamination length, we consider the energy required to advance the delamination. Specifically, we exploit the J -integral:

$$J = \oint_{\Omega} \left(\mathcal{W} n_x - \sigma_{ij} n_j \frac{du_i}{dx} \right) d\Omega, \quad (2.7)$$

to calculate the energy release rate [53], where $\mathbf{n} = (n_x, n_z)$ is the outward-pointing normal vector to the path, \mathcal{W} denotes the strain energy density, and σ_{ij} and u_i represent the stress and displacement components, respectively. We examine the integral over a path Ω right near the delamination front (see the inset in Fig. 1), which is decomposed as $\Omega = \Omega_1 \cup \Omega_2 \cup \Omega_3 \cup \Omega_4$. Proceeding with the linear plate theory and the combined foundation model in Eq. (2.1), we obtain:

$$J = \left(p w - \frac{p^2}{2k_w} + \frac{p'^2}{2k_1} \right) \Big|_{x=\ell^+}. \quad (2.8)$$

We limit our analysis by neglecting the mode-mixity [54,55] and consider a constant adhesion energy or interface toughness γ . This leads to a discontinuity condition at the delamination front:

$$\left[\left[p(\ell) w(\ell) - \frac{p^2(\ell)}{2k_w} + \frac{p'^2(\ell)}{2k_1} \right] \right] = \gamma. \quad (2.9)$$

Lastly, similar to a typical contact mechanics problem [15], we still lack one final condition, which might be physically informed. As discussed in the literature, two potential choices are available: $\llbracket w''''(\ell) \rrbracket = 0$ (i.e., $\llbracket p(\ell) \rrbracket = 0$) to ensure high-order continuity, or $\llbracket w''''(\ell) \rrbracket = 0$ (i.e., $\llbracket p'(\ell) \rrbracket = 0$) to ensure that the pressure becomes maximally tensile at the delamination front [14]. We first adopt the former condition and will compare these two options in the next section, demonstrating that the difference is just quantitative as long as Eq. (2.9) is consistently applied. Specifically, under the first choice, we have:

$$\llbracket w''''(\ell) \rrbracket = 0 \quad \text{and} \quad \llbracket w''''(\ell) \rrbracket = 2k_1 \gamma / B^2. \quad (2.10)$$

As such, the problem of Eq. (2.4) subject to (2.5), (2.6), and (2.10) can be analytically solved.

2.2. Non-dimensionalization

We next discuss the characteristic lengths in the system before non-dimensionalization. To relate the length scale ℓ in the delamination

region (i.e., $0 < x < \ell$) to the intrinsic properties of the system, we compare the elastic energy stored in the plate, $\sim B \delta^2 / \ell^4 \times \ell$, with the adhesion energy, $\sim \gamma \times \ell$. This yields a bendoadhesive or elastocapillary length [51]:

$$\ell_{ec} = (B \delta^2 / \gamma)^{1/4}. \quad (2.11)$$

In the contact region (i.e., $x > \ell$), there are two horizontal length scales to characterize the region over which the lifted deflection smears out [56,57], depending on whether the volume-changing or the shape-changing deformation dominates. When the former dominates, the classical Winkler length is obtained:

$$\ell_w = \left(\frac{B}{k_w} \right)^{1/4} = \left[\frac{(1-2\nu)Bd}{2(1-\nu)G} \right]^{1/4}. \quad (2.12)$$

Alternatively, for relatively incompressible elastic layers [27], $\ell_w \rightarrow 0$ and the characteristic length is instead given by:

$$\ell_1 = \left(\frac{B}{k_1} \right)^{1/6} = \left[\frac{(3/4 - \nu)(\nu - 1/4)Bd^3}{3(1-\nu)^2 G} \right]^{1/6}. \quad (2.13)$$

We then compare the two horizontal length scales to obtain:

$$\epsilon = \left(\frac{\ell_w}{\ell_1} \right)^6 = (1-2\nu)^{3/2} \frac{3(1-\nu)^{1/2}}{2^{3/2}(3/4 - \nu)(\nu - 1/4)} \left(\frac{B}{Gd^3} \right)^{1/2}, \quad (2.14)$$

which can be interpreted as the effective compressibility of the thin elastic layer [27]. Notably, in typical experiments such as Ref. [14], both the modulus and thickness of the plate are much greater than those of the adhesive layer (i.e., $B \gg Gd^3$). This implies that $\epsilon \ll 1$ in general, unless the Poisson's ratio of the thin layer is extremely close to 1/2.

We then use lifted deflection δ and the Winkler length ℓ_w as rescaling parameters. Specifically, we define the following dimensionless variables:

$$X = x / \ell_w, \quad L = \ell / \ell_w, \quad W = w / \delta, \quad (2.15)$$

and a dimensionless (effective) adhesion

$$\Gamma = \frac{\gamma \ell_w^4}{B \delta^2} = \frac{\gamma}{k_w \delta^2}. \quad (2.16)$$

With these, the problem specified in Eqs. (2.4), (2.5), (2.6), and (2.10) becomes

$$\epsilon^{-1} W'''''' \mathcal{H}(X - L) - W'''' - W \mathcal{H}(X - L) = 0, \quad (2.17)$$

subject to boundary conditions:

$$W(0) = 1, \quad W''(0) = 0, \quad W(\infty) = 0, \quad W'(\infty) = 0, \quad W''(\infty) = 0, \quad (2.18)$$

continuity conditions:

$$\llbracket W(L) \rrbracket = \llbracket W'(L) \rrbracket = \llbracket W''(L) \rrbracket = \llbracket W'''(L) \rrbracket = \llbracket W''''(L) \rrbracket = 0, \quad (2.19)$$

and a jump condition:

$$\llbracket W''''''(L) \rrbracket = 2\epsilon \Gamma, \quad (2.20)$$

where $W' = dW/dX$ in this section. After the non-dimensionalization, the problem only relies on two parameters: the effective material compressibility ϵ and the effective adhesion Γ . Note again, $\epsilon^{-1} \ll 1$ in Eq. (2.17) except for extremely incompressible materials.

2.3. Analytical solutions

2.3.1. The general solution

We then discuss some analytic progress that can be made. The analytical solution in the delamination region is simple. The solution in the contact region can be identified by acknowledging that it is identical to the solution of $W'' = \lambda^2 W$ if λ satisfies $\lambda^6 / \epsilon - \lambda^4 - 1 = 0$.

We then obtain three pairs of roots: $\lambda^2 = \lambda_1^2, \lambda_2^2$, and λ_3^2 . For $\epsilon > 0$, there is only one pair of real root denoted as $\pm\lambda_1$, given by

$$\lambda_1 = \frac{1}{3^{1/2}} \left[\epsilon + \frac{\epsilon^2}{f(\epsilon)} + f(\epsilon) \right]^{1/2}, \quad (2.21)$$

where $f(\epsilon) = \left[\epsilon^3 + 3 \left(9\epsilon + \sqrt{81\epsilon^2 + 12\epsilon^4} \right) / 2 \right]^{1/3}$. We represent the rest two pairs of complex roots $\lambda_2^2 = -\lambda_R + \lambda_I i$ and $\lambda_3^2 = -\lambda_R - \lambda_I i$ by their argument and the modulus, i.e.,

$$\theta = \arctan \left[\frac{\sqrt{3}f^2(\epsilon) - \sqrt{3}\epsilon^2}{f^2(\epsilon) + \epsilon^2 - 2\epsilon f(\epsilon)} \right] \quad (2.22)$$

and

$$\Lambda = \frac{1}{3^{1/2}f^{1/2}(\epsilon)} \left[(f^3(\epsilon) - \epsilon^3)(f(\epsilon) - \epsilon) \right]^{1/4}, \quad (2.23)$$

respectively. Using these and the boundary/continuity conditions, we obtain the solution to Eq. (2.17):

$$\begin{aligned} W(X) = & (C_1 X^3 + C_2 X + 1) \mathcal{H}(L - X) \\ & + \left[C_3 \exp(-\lambda_1 X) + \exp\left(-\Lambda \sin \frac{\theta}{2} X\right) \left(C_4 \cos \frac{\Lambda \theta X}{2} + C_5 \sin \frac{\Lambda \theta X}{2} \right) \right] \\ & \times \mathcal{H}(X - L), \end{aligned} \quad (2.24)$$

where the constants C_1, C_2, C_3, C_4 , and C_5 depend on $\lambda_1(\epsilon), \Lambda(\epsilon), \theta(\epsilon)$, and $L(\epsilon, \Gamma)$ (see detailed expressions in Appendix A). This solution is new to the best of our knowledge.

We can then calculate the dimensionless force required to achieve such a peeling state by performing a shear force balance at the end of the plate:

$$F = \frac{F_{\text{ec}}}{B\delta} = F \left(\frac{\delta^2}{B\gamma^3} \right)^{1/4} = \frac{3\lambda_1^2 \Lambda^3}{g(\lambda_1, \Lambda, \theta, L) \Gamma^{3/4}}, \quad (2.25)$$

where

$$\begin{aligned} g(\lambda_1, \Lambda, \theta, L) = & \left[6\lambda_1^2 + 12\lambda_1 \Lambda (1 + \lambda_1 L) \sin \frac{\theta}{2} + 6(1 + \lambda_1 L)^2 \Lambda^2 \right] \sin \frac{\theta}{2} \\ & + \Lambda \Lambda^3 (3 + 3\Lambda \lambda_1 + L^2 \lambda_1^2). \end{aligned} \quad (2.26)$$

Note that we have adopted ℓ_{ec} to define the dimensionless peeling force [58,59], because the peeling force for a plate on a rigid substrate is given by:

$$F_{\text{rigid}} = (8/9)^{1/4}. \quad (2.27)$$

As the delamination propagates, the system would eventually reach a steady state in which the effect of the thin layer elasticity becomes negligible [25]. We thus expect that F approaches F_{rigid} as L increases.

It should also be noted that the delamination length L is part of the solution. It can be calculated according to the delamination condition in Eq. (2.20), i.e.,

$$\Gamma = \frac{1}{2\epsilon} \left[\frac{\lambda_1 \left(2 \sin \frac{\theta}{2} + \Lambda L \right) + \Lambda}{g(\lambda_1, \Lambda, \theta, L) / (3\lambda_1^2 \Lambda^4)} \right]^2. \quad (2.28)$$

The delamination length L then depends on both the compressibility of the thin layer ϵ and the effective adhesion Γ , which further relies on the lifted height, foundation stiffness, and adhesion energy according to Eq. (2.16). Similarly, inspired by the steady state or the rigid case, we will discuss the delamination length via

$$\mathcal{L} = \ell / \ell_{\text{ec}} = \Gamma^{1/4} L, \quad (2.29)$$

since the classical result given by Obreimoff [60]

$$\mathcal{L}_{\text{rigid}} = (9/2)^{1/4}. \quad (2.30)$$

Therefore, for a given Γ , we are able to calculate the delamination length based on Eq. (2.28) and the required peeling force based on

Eq. (2.25) for thin layers with arbitrary compressibility ϵ . In addition, as $\Gamma \ll 1$, we expect $L \gg 1$ and $F \rightarrow F_{\text{rigid}}$ and $\mathcal{L} \rightarrow \mathcal{L}_{\text{rigid}}$, regardless of the material compressibility. However, we will show that the solution for the delamination length L in Eq. (2.28) does not always exist, particularly when Γ is large. Physically, this means that with a large Γ (i.e., a strong adhesion, a soft foundation, or a small lifted deflection), the interface does not delaminate at all. In this case, the analytical solution given by Eq. (2.20) remains valid simply by setting $L = 0$, while the dimensionless peeling force simplifies as

$$F(L=0) = \frac{\lambda_1^2 \Lambda^3 \csc \frac{\theta}{2}}{2 \left(2\lambda_1 \Lambda \sin \frac{\theta}{2} + \lambda_1^2 + \Lambda^2 \right)} \cdot \frac{1}{\Gamma^{3/4}}. \quad (2.31)$$

Such a no-delamination solution differs fundamentally from the delamination solution (2.25). This can be illustrated in a dimensionless form: before delamination occurs, Eq. (2.31) suggests $F \propto \delta$, while after delamination occurs, Eq. (2.25) instead approximately suggests $F \propto \delta^{-1/2}$. This contrast will be further illustrated in Figs. 2 and 3.

2.3.2. The perfectly compressible limit: $\epsilon \rightarrow \infty$

In Fig. 2, we present the delamination lengths and peeling forces as functions of the effective adhesion Γ for thin layers with varying compressibilities ϵ (indicated by the color bar). As anticipated, for very small Γ , the delamination length becomes large, and the system approaches a steady state regardless of ϵ : The peeling behavior of the plate from the thin elastic layer resembles peeling from a rigid substrate, characterized by $\mathcal{L}_{\text{rigid}} = (9/2)^{1/4}$ and $F_{\text{rigid}} = (8/9)^{1/4}$. For a finite Γ , the peeling force F slightly exceeds F_{rigid} , while the delamination length \mathcal{L} could be much smaller than $\mathcal{L}_{\text{rigid}}$. Furthermore, when the effective adhesion Γ becomes sufficiently large, delamination does not occur and $L = 0$. In this case, the dimensional force-deflection relationship given by Eq. (2.31) is linear, as indicated by the dotted lines in Fig. 2b and discussed shortly in Eq. (2.37).

Fig. 2 suggests that the compressibility of the thin layer influences the delamination behavior. However, for sufficiently compressible layers (i.e., $\epsilon \gg 1$), both the $\mathcal{L}-\Gamma$ and $F-\Gamma$ relations converge onto master curves corresponding to the perfectly compressible limit. Specifically, as $\epsilon \rightarrow \infty$, we find:

$$\lambda_1 \rightarrow \infty, \quad \Lambda \rightarrow 1, \quad \text{and} \quad \theta \rightarrow \pi/2, \quad (2.32)$$

according to Eqs. (2.21), (2.22), and (2.23). At this perfectly compressible limit, the critical adhesion energy below which the interface starts to delaminate is given by $\Gamma_{\text{cr}} = 1/2$. This corresponds to a dimensional critical lifted deflection:

$$\delta_{\text{cr}} = \sqrt{\frac{2\gamma}{k_{\text{w}}}} = \sqrt{\frac{(1-2\nu)\gamma d}{(1-\nu)G}}. \quad (2.33)$$

Similarly, the critical peeling force is $F_{\text{cr}} = 2^{1/4} = \sqrt{3/2} F_{\text{rigid}}$ and its dimensional form reads:

$$F_{\text{cr}} = \left(\frac{2B\gamma^3}{\delta^2} \right)^{1/4} = \left[\frac{2(1-\nu)BG\gamma^2}{(1-2\nu)d} \right]^{1/4}. \quad (2.34)$$

This clearly suggests the critical peeling force for the delamination to occur is affected by not only the intrinsic adhesion toughness but also the mechanical properties of the systems, including the thickness, Poisson's ratio, and shear modulus of the adhesive layers [13].

After the delamination takes place, the delamination length at the perfectly compressible limit is given by

$$\ell = \left[\frac{2^{3/4} k_{\text{w}}^{1/4} \delta^{1/2}}{\gamma^{1/4}} \sin \left(\frac{1}{3} \arctan \sqrt{\frac{k_{\text{w}}^{3/2} \delta^3}{2^{1/2} \gamma^{3/2}} - 1} + \frac{\pi}{6} \right) - \sqrt{2} \right] \left(\frac{B}{k_{\text{w}}} \right)^{1/4}, \quad (2.35)$$

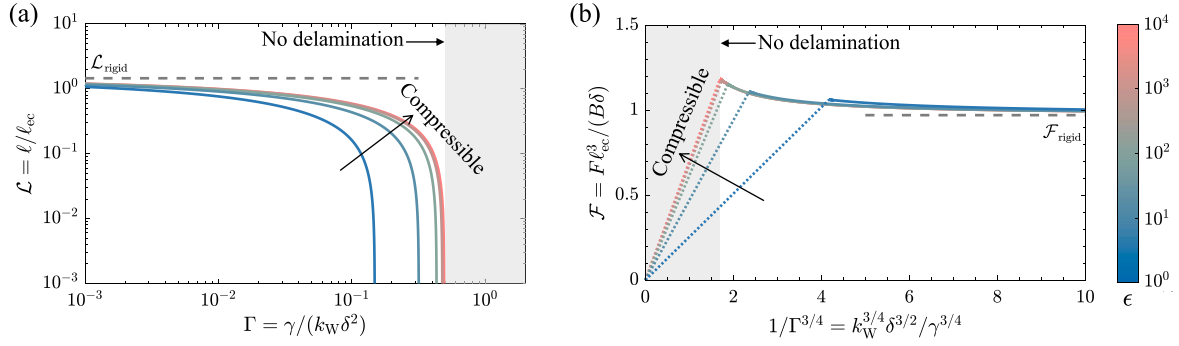


Fig. 2. Peeling a flexible plate from a thin elastic layer with increasing compressibility that is characterized by ϵ in Eq. (2.14). (a) Dimensionless delamination length \mathcal{L} defined in (2.29) as a function of the effective adhesion energy Γ defined in (2.16). (b) Dimensionless peeling force \mathcal{F} defined in (2.25) as a function of $\Gamma^{-3/4}$. The colored solid curves correspond to the analytical solutions given by Eqs. (2.25) and (2.28). The dotted lines in (b) are based on Eq. (2.31), indicating that delamination has not yet occurred. The dashed lines in (a) and (b) are given by the steady state, i.e., (2.27) and (2.30), respectively. The gray-shaded regions represent the no-delamination regime at $\epsilon \rightarrow \infty$ (i.e., the perfectly compressible limit).

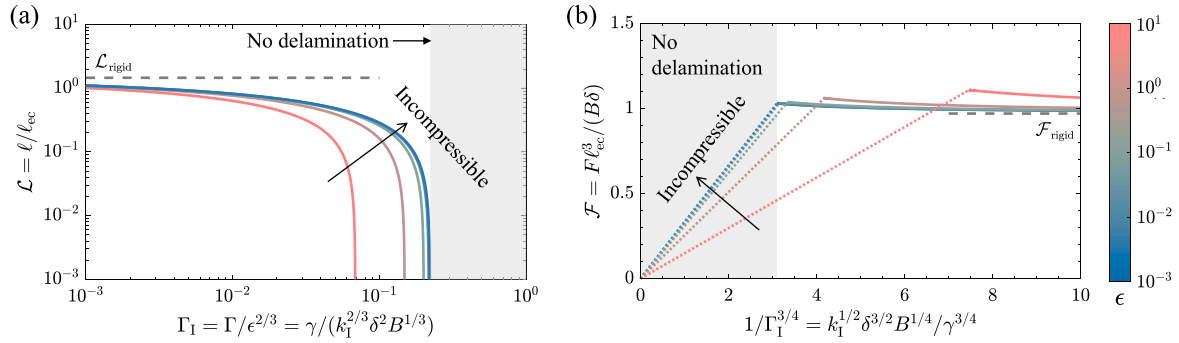


Fig. 3. Peeling a flexible plate from a thin elastic layer with increasing incompressibility characterized by ϵ^{-1} . (a) Dimensionless delamination length \mathcal{L} defined in (2.29) as a function of the effective adhesion energy Γ defined in (2.16). (b) Dimensionless peeling force \mathcal{F} defined in (2.25) as a function of $\Gamma^{-3/4}$. Again, the colored solid curves correspond to the delamination solution Eqs. (2.24) and (2.28) while dotted lines in (b) correspond to the no-delamination solution Eq. (2.31). The dashed lines in (a) and (b) are given by (2.27) and (2.30), respectively. The gray-shaded regions represent the no-delamination regime at $\epsilon \rightarrow 0$ (i.e., the perfectly incompressible limit).

which could be further simplified as

$$\ell = \begin{cases} 0, & \text{for } \delta \leq \delta_{\text{cr}} \\ (1 - \delta_{\text{cr}}^2/\delta^2) (B/4k_W)^{1/4}, & \text{for } 0 \leq \delta - \delta_{\text{cr}} \ll \delta_{\text{cr}} \\ (3^{1/2} - 2^{1/4} \delta_{\text{cr}}^{1/2}/\delta^{1/2}) (B\delta^2/2\gamma)^{1/4}, & \text{for } \delta \gg \delta_{\text{cr}}. \end{cases} \quad (2.36)$$

In addition, the dimensional peeling force as a function of the lifted deflection at the edge of the plate can be given by

$$F = \begin{cases} B\delta / (\sqrt{2}\ell_W^3), & \text{for } \delta \leq \delta_{\text{cr}} \\ 3B\delta / (\ell^3 + 3\sqrt{2}\ell_W\ell^2 + 6\ell_W^2\ell + 3\sqrt{2}\ell_W^3), & \text{for } \delta > \delta_{\text{cr}}. \end{cases} \quad (2.37)$$

This suggests a linear peeling force–deflection relation before the delamination while the peeling force starts to decrease with the lifted deflection after the delamination (since ℓ is roughly proportional to $\delta^{1/2}$). Note that to reach these simple expressions, we have used the Winkler length ℓ_W to rescale the system, which is consistent with the compressible limit $\epsilon \gg 1$. To understand the delamination behavior for systems of $\epsilon \ll 1$, however, it is more appropriate to use ℓ_1 for rescaling, which we discuss below.

2.3.3. The perfectly incompressible limit: $\epsilon \rightarrow 0$

As $\nu \rightarrow 1/2$, the Winkler length ℓ_W approaches zero. In this context, we need to replace ℓ_W with the incompressible length ℓ_1 in Eq. (2.16) to define the incompressible version of effective adhesion energy, namely,

$$\Gamma_1 = \frac{\Gamma}{\epsilon^{2/3}} = \frac{\gamma}{B^{1/3}k_1^{2/3}\delta^2}. \quad (2.38)$$

In Fig. 3, we plot the dimensionless delamination length and peeling force as functions of Γ_1 based on Eqs. (2.25) and (2.28) for thin layers of various ϵ and Γ . It is evident that, as $\epsilon \ll 1$, the curves converge, indicating that Γ_1 is the sole controlling parameter in the perfectly incompressible limit. Remarkably, unlike Γ for perfectly compressible layers, Γ_1 for perfectly incompressible layers is influenced not only by the substrate elasticity but also by its bending stiffness. We will demonstrate that this dependence on the plate's properties can be exploited to assess the effective compressibility of a thin layer in experiments.

To gain a quantitative understanding of the delamination behavior in the perfectly incompressible limit, we apply $\epsilon \rightarrow 0$ to Eqs. (2.21), (2.22), and (2.23), obtaining $\lambda_1 \rightarrow \epsilon^{1/3}$, $\Lambda \rightarrow \epsilon^{1/3}$, and $\theta \rightarrow \pi/3$. The critical adhesion energy is given by $\Gamma_1 = 2/9$, i.e., that the critical lifted deflection for delamination to occur is

$$\delta_{\text{cr}} = \left[\frac{9(3/4 - \nu)(\nu - 1/4)}{2^{3/2}(1 - \nu)^2} \right]^{1/3} \frac{\gamma^{1/2}d}{B^{1/6}G^{1/3}}. \quad (2.39)$$

The critical peeling force is slightly greater than the steady-state force: $F_{\text{cr}} = (9/8)^{1/4} \approx 1.06 F_{\text{rigid}}$, corresponding to

$$F_{\text{cr}} = \frac{B^{1/3}G^{1/6}\gamma^{1/2}}{d^{1/2}} \left[\frac{6(1 - \nu)^2}{(3 - 4\nu)(4\nu - 1)} \right]^{1/6}. \quad (2.40)$$

At this perfectly incompressible limit, the delamination length is given by

$$\ell = \left[\left(\frac{1}{2} \sqrt{1 - \frac{\sqrt{2}B^{1/2}k_1\delta^3}{\gamma^{3/2}}} - \frac{1}{2} \right)^{1/3} + \frac{B^{1/6}k_1^{1/3}\delta}{64\gamma^{1/2}} \left(\sqrt{1 - \frac{\sqrt{2}B^{1/2}k_1\delta^3}{\gamma^{3/2}}} - 1 \right)^{-1/3} - 2 \right] \times \left(\frac{B}{k_1} \right)^{1/6}, \quad (2.41)$$

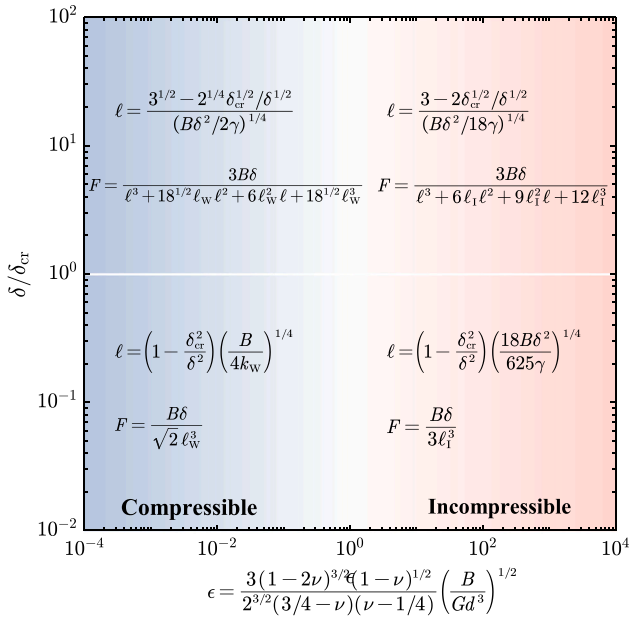


Fig. 4. A regime diagram for peeling from elastomeric layers with different compressibilities. The asymptotic behavior of the detachment length and the peeling force can be found in different $\{\epsilon, \delta\}$ space.

which can be simplified as

$$\ell = \begin{cases} 0, & \text{for } \delta \leq \delta_{cr} \\ (1 - \delta_{cr}^2/\delta^2)^{1/4} (18B\delta^2/625\gamma)^{1/4}, & \text{for } 0 \leq \delta - \delta_{cr} \ll \delta_{cr} \\ (3 - 2\sqrt{\delta_{cr}/\delta}) (B\delta^2/18\gamma)^{1/4}, & \text{for } \delta \gg \delta_{cr}. \end{cases} \quad (2.42)$$

The dimensional peeling force for various lifted deflections is given by

$$F = \begin{cases} B\delta/(3\ell_l^3), & \text{for } \delta \leq \delta_{cr} \\ 3B\delta/(\ell^3 + 6\ell_l\ell^2 + 9\ell_l^2\ell + 12\ell_l^3), & \text{for } \delta > \delta_{cr}, \end{cases} \quad (2.43)$$

before and after the delamination.

Having examined the effect of compressibility on peeling behavior, we summarize our analytical findings in a regime diagram in Fig. 4. This diagram, constructed based on the compressibility of the elastic layer and the lift-off height during peeling, allows for the quick identification of the two most critical physical quantities in the delamination process—the detachment length and the peeling force.

These results complete our analytical solutions derived under the assumption of zero pressure at the delamination front. However, it remains unclear whether the zero pressure or zero pressure gradient assumption provides a better approximation. To resolve this, we also solve the problem by assuming a zero pressure gradient at the delamination front. In this case, the matching condition in Eq. (2.10) becomes

$$\left[w''''(\ell) \right] = 0 \quad \text{and} \quad \left[2kw(\ell)w''''(\ell) + Bw'''(\ell) \right] = 2k_w\gamma/B, \quad (2.44)$$

according to the generalized energy release rate in Eq. (2.8). Using the same process and non-dimensionalization as in this section, we can calculate the deflection of the plate, the delamination length, and the required peeling force for thin layers with arbitrary compressibilities under the assumption of zero pressure gradient at the delamination front (see detailed expressions in Appendix B). We then compare the two sets of solutions with more specific cohesive zone model simulations.

2.4. Comparison with finite element analysis

We employ a cohesive zone model to simulate the interface delamination problem using the finite element method (FEM) [61,62].

Following the experimental parameters reported in Ref. [14], we consider a glass plate on a relatively soft polymeric layer, with the bottom surface perfectly bonded (Fig. 1). A typical bilinear cohesive law is adopted, with a fracture energy of $\gamma = 40 \text{ mJ/m}^2$ (see details in Appendix C). The substrate is modeled using a neo-Hookean material with a shear modulus of $G = 0.5 \text{ MPa}$ and a thickness of $d = 50 \text{ }\mu\text{m}$, while the linearly elastic plate has a bending rigidity of $B = 9 \times 10^{-4} \text{ N m}$ in our computations. We use different lifted deflection δ to tune the effective adhesion energy Γ and vary the Poisson's ratio ν to regulate the effective compressibility of the substrate ϵ . Note that the validity of the combined foundation model in Eq. (2.1) requires the substrate to have a large slenderness ratio, i.e., $d \ll \max\{\ell_w, \ell_l\}$, which is equivalent to

$$S = \max \left\{ \frac{(1-2\nu)B}{2(1-\nu)Gd^3}, \frac{(3/4-\nu)(\nu-1/4)B}{3(1-\nu)^2Gd^3} \right\} \gg 1. \quad (2.45)$$

This requirement is satisfied in our FEM model, where $S \sim 10^4$.

2.4.1. A nearly compressible case

We first consider a nearly compressible case in Fig. 5a and b, where the substrate has a Poisson's ratio of 0.35, corresponding to an effective compressibility $\epsilon = 425$. Interestingly, no significant difference is observed between solutions obtained with $p(\ell) = 0$ (denoted by solid curves) and $p'(\ell) = 0$ (denoted by dotted curves), even in the regime where delamination has not yet been initiated (see the shaded regime in Fig. 5b). Additionally, the analytical results show excellent agreement with the cohesive zone modeling calculations (denoted by markers), except in a small region near $\Gamma = \Gamma_{cr}$, i.e., the very early stage of delamination. This minor deviation is acceptable, as in this stage $L \ll 1$, and the finite size of the process zone caused by using the cohesive zone model can play a role but is not considered in our analytical model [63]. As the delamination propagates, both sets of analytical results are quite accurate in predicting the length of the delamination and the peeling force of the system, particularly how they approach the steady state (see the inset in Fig. 5a).

To understand the vanishing difference between analytical solutions based on two distinct continuity conditions, we examine the interaction pressures between the plate and the thin layer in two configurations: one without cracks (Fig. 5c) and the other with a pre-existing crack of length $\ell = 5d$ (Fig. 5d), where d is the thickness of the thin layer. The plate and thin layer are directly bonded without cohesive elements. The geometric and material parameters are identical to those described above in the finite element model. From Fig. 5c and d, we observe that the pressure distribution between the analytical model with $p(\ell) = 0$, the analytical model with $p'(\ell) = 0$, and the numerical results only differ significantly in a small region, no matter whether there is a pre-existing crack or not. The size of this boundary layer, suggested by Eq. (2.17), is $\sim \epsilon^{1/6}$, which is small when $\epsilon \gg 1$.

The evaluation of the energy release rate, or the J -integral, however, depends directly on the pressure and its gradient within the boundary layer. We then compare the results obtained using the reduced foundation model with Eq. (2.8) to the 3D FEM calculation using the original Eq. (2.7). We find that, in the absence of cracks ($\ell = 0$), the error relative to the FEM result in J evaluated at the edge is only 8.6% for the foundation model using $p(\ell) = 0$ and 4.6% for the model using $p'(\ell) = 0$. In the case of a pre-existing crack ($\ell = 5d$), the errors are even smaller: 5.6% and 3.1%, respectively. Therefore, in this nearly compressible case, it does not matter whether we choose the zero pressure or zero pressure gradient condition to solve the problem, as long as the generalized J in Eq. (2.8) is consistently used.

2.4.2. A nearly incompressible case

We now consider a nearly incompressible case in Fig. 6a and b, where the substrate has a Poisson's ratio of 0.499, corresponding to an effective compressibility $\epsilon = 0.13$. Surprisingly, at small $\Gamma_1 = \Gamma/\epsilon^{2/3}$, the delamination length and the peeling force calculated with zero

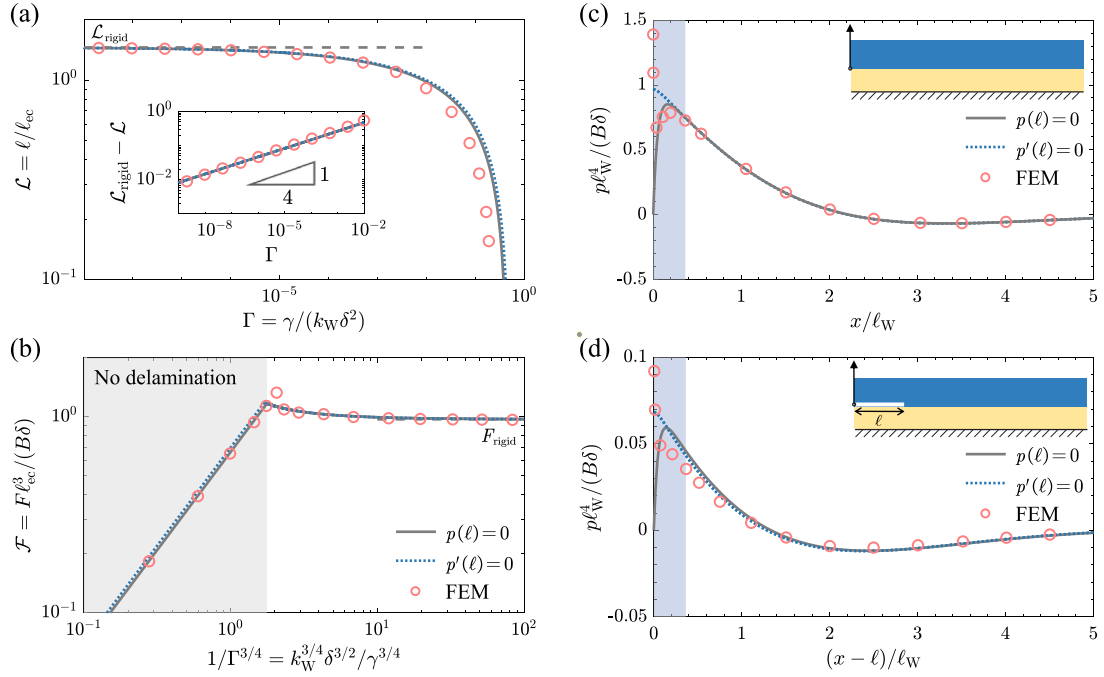


Fig. 5. Comparison of analytical results and cohesive zone modeling simulations in the nearly compressible case. (a, b) The dimensionless delamination length (a) and peeling force (b) as functions of the effective adhesion energy Γ . (c, d) The dimensionless surface traction $p\ell_W^4/(B\delta)$ acting on the thin layer bonded to the plate, without a pre-existing crack (c) and with a pre-existing crack of length $\ell = 5d$ (d). In all panels, the solid curves represent the analytical results obtained by enforcing the continuity of the surface normal traction (i.e., zero pressure) at the delamination front, while the dotted curves correspond to results derived by assuming that the normal traction at the delamination point reaches its maximum (i.e., zero pressure gradient). The markers represent results from finite element calculations with $\epsilon = 425$. The gray-shaded region in (b) denotes the no-delamination regime. The blue-shaded region in (c) and (d) indicates a boundary layer region, $0 \leq X \leq 1/\epsilon^{1/6}$. Note that an interfacial cohesive layer is used in the FEM calculations in (a) and (b), but not in (c) and (d).

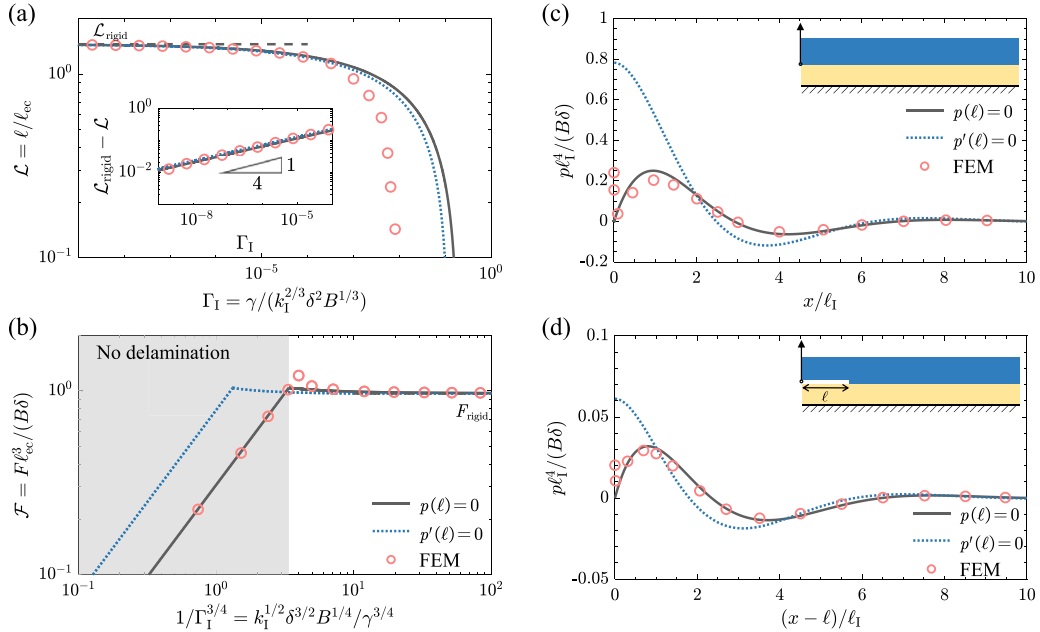


Fig. 6. Comparison of analytical results and cohesive zone modeling simulations in the nearly incompressible case. (a, b) The dimensionless delamination length (a) and peeling force (b) as functions of the effective adhesion energy $\Gamma_I = \Gamma/\epsilon^{2/3}$. (c, d) The dimensionless surface traction $p\ell_I^4/(B\delta)$ acting on the thin layer bonded to the plate, without a pre-existing crack (c) and with a pre-existing crack of length $\ell = 5d$ (d). In all panels, the solid curves represent the analytical results obtained by enforcing zero pressure at the delamination front while the dotted curves correspond to results derived by assuming a zero pressure gradient. The markers represent results from finite element calculations with $\epsilon = 0.13$. The gray-shaded region in (b) denotes the no-delamination regime. Again, an interfacial cohesive layer is used in the FEM calculations in (a) and (b), but not in (c) and (d).

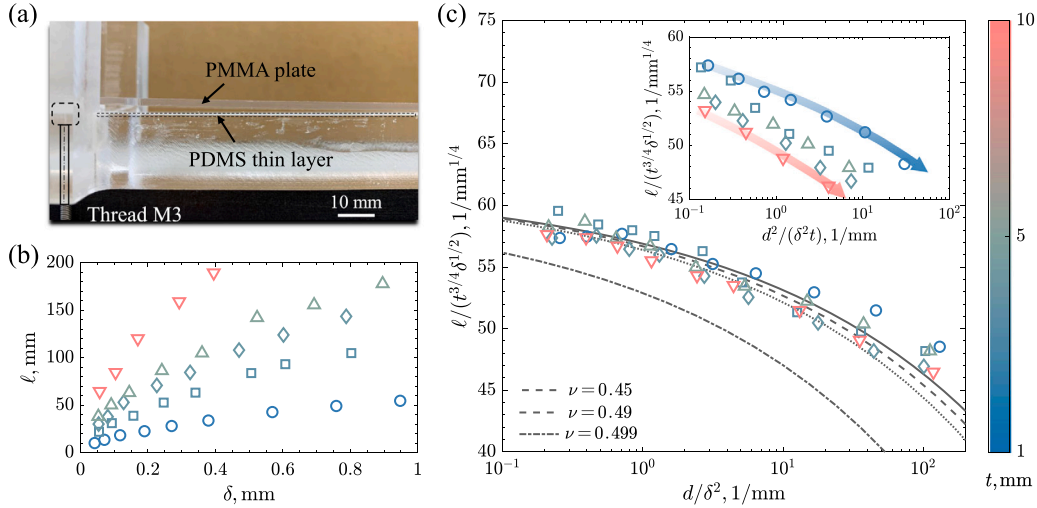


Fig. 7. A compressibility test. (a) Photograph of the experimental setup following the illustration in Fig. 1. (b) Measured delamination length for peeling an acrylic plate from a thin PDMS layer. The marker color represents the thickness of the plate as encoded in the color bar. (c) Rescaled delamination length as a function of d/δ^2 . The solid curve represents the analytical solution (2.35) for the perfectly compressible limit with an adhesion energy 72 mJ/m^2 . The inset shows the rescaled delamination length as a function of $d^2/(\delta^2 t)$.

pressure and zero pressure gradient at the delamination front are nearly identical, and both agree well with the FEM results. However, at relatively large Γ_1 , particularly near and before the onset of delamination, both solutions deviate from the FEM results while the zero-pressure solution remains good in predicting the peeling force (see Fig. 6b). This can be further understood by examining the pressure distribution at the plate-layer interface, calculated with and without a pre-existing crack (Fig. 6c and d). Compared with the continuity of the pressure gradient, the analytical solution obtained by enforcing the continuity of pressure shows much better agreement with the FEM results in both configurations.

It should be noted, however, that neither the zero pressure nor the zero pressure gradient condition is strictly required or fully appropriate from the perspective of boundary layer analysis [64]. It just happens that the approximation with the zero pressure condition does not deviate significantly in this 1D setup.

Therefore, we may conclude, based on the comparison between the nearly compressible and incompressible cases, that the condition of zero pressure, or more generally the continuity of w'''' , can provide a good approximation for the peeling of the plate from a thin layer of arbitrary compressibility. Nonetheless, the difference between the zero pressure and zero pressure gradient conditions in predicting the delamination length and peeling force is small as delamination progresses. Indeed, the difference between the zero pressure and zero pressure gradient conditions is small for various values of ϵ (see the discussions in Appendix D). In addition, as shown in Fig. D.9, the J -integral approach is essentially identical to the energy approach (which minimizes the total free energy with respect to the delamination length). However, the approach introduced here provides a direct jump condition at the delamination front, making analytical solutions to the problem of arbitrary compressibility more tractable.

3. Does compressibility matter?

We now attempt to answer the question we posed earlier: Does the material compressibility matter in the delamination behavior of thin adhesive layers? The answer, suggested by the results in the preceding section, is clearly yes. Furthermore, we have shown that ϵ defined in Eq. (2.14) can provide a measure of the effective compressibility, the combined foundation model given in Eq. (2.1) can characterize the deformation of thin layers with varying ϵ , and the J -integral evaluated in Eq. (2.7) can be used to approximate the energy release

rate. However, we emphasize that achieving $\epsilon \ll 1$ could be very challenging in experiments where the plate is much stiffer or thicker than the adhesive thin layer unless the Poisson's ratio of the adhesive approaches 0.5. To illustrate this point, we test polydimethylsiloxane (PDMS) elastomeric layers, which are generally regarded as nearly incompressible: $0.45 \lesssim \nu \lesssim 0.5$ [40].

As shown in Fig. 7a, the experimental setup follows the schematic in Fig. 1, as reported in Ref. [14]. The elastic PDMS layer is prepared by mixing the base polymer and curing agent in a ratio of 10:0.9, thoroughly stirring the mixture, and subsequently placing it in a vacuum chamber to eliminate air bubbles. The PDMS solution is then evenly coated onto an acrylic substrate and cured at 80°C for two hours. After curing, a PMMA thin plate is adhered to the PDMS surface. A rectangular hole is machined into an acrylic block to serve as a sliding track, and an M3 screw is threaded at the center of the acrylic base. By turning the screw very slowly to avoid any rate-dependent effect, the slider can be moved up or down, thereby applying displacement δ to the acrylic plate above. The screw has a thread pitch of 0.5 mm, which means that for every 90° rotation of the screw, the slider rises by approximately 0.125 mm.

An interesting result of our analytical solutions at the perfectly compressible and incompressible limits is the exclusive dependence of their delamination behavior, such as $\mathcal{L} = \ell \gamma^{1/4}/(B^{1/4}\delta^{1/2})$, on $\Gamma \sim \gamma d/(G\delta^2)$ and $\Gamma/\epsilon^{2/3} \sim \gamma d^2/(G^{2/3}B^{1/3}\delta^2)$, respectively. This implies that the compressibility or incompressibility of the thin layer can be inferred simply by examining how the delamination length depends on the properties of the flexible plates. In particular, for a plate with thickness t , the rescaled delamination length $\ell/(t^{3/4}\delta^{1/2})$ depends on d/δ^2 for perfectly compressible layers, but on $d^2/(\delta^2 t)$ for perfectly incompressible layers. We then make use of this distinct dependence on the plate thickness in our experiments, as this approach is highly practical and does not require any force measurements.

The peeling experiments are performed on 100–300 μm -thick PDMS thin layers using flexible plates of thicknesses 1 mm, 2 mm, 4 mm, 5 mm, and 10 mm. Fig. 7b shows the experimentally measured delamination length ℓ as a function of the lifted height δ for plates of various thicknesses. The delamination length exhibits an approximately square root relation with δ . We then plot the scaled delamination length $\ell/(t^{3/4}\delta^{1/2})$ as a function of d/δ^2 and $d^2/(\delta^2 t)$ in Fig. 7c and its inset, respectively. The good collapse of the data in Fig. 7c suggests the relative independence of the rescaled delamination length on the plate

thickness, i.e., that the PDMS layer appears compressible rather than incompressible in the peeling experiments. Notably, the analytical solution in the perfectly compressible limit, Eq. (2.35), with an adhesion energy of 72 mJ/m^2 , provides an excellent fit to the experimental results.

To further elucidate the effect of compressibility, we performed additional finite element simulations for experiments with varying substrate Poisson's ratios. The results show that when the Poisson's ratio is below 0.49, the simulations closely match both the compressible limit and the experimental data. However, at a Poisson's ratio of 0.499, the simulations exhibit pronounced incompressibility, resulting in noticeable deviations from experimental observations. These findings indicate that, despite being nearly incompressible in bulk form, the thin elastomeric layer in our experiments exhibit compressible behavior. The results in Fig. 7 can be readily explained by the effective compressibility ϵ defined in Eq. (2.14). Even with a Poisson's ratio of $\nu = 0.49$ for the PDMS layer, the calculated compressibility remains large, ranging from 10.1 to 99.2 as the plate thickness increases from 1 mm to 10 mm. This highlights the importance of caution when applying the perfectly incompressible limit to adhesion bonding problems: Even nearly incompressible materials may behave compressibly when confined within slender geometries.

4. Conclusions

Motivated by the concern that neither the perfectly compressible nor the perfectly incompressible model is fully applicable to elastomeric adhesive layers, this study has investigated the peeling of a flexible plate from an adhesive layer with arbitrary compressibility. We have discussed the appropriate reduced foundation model and related matching conditions and jump conditions due to the presence of adhesive forces. There are several findings in this study that could be of importance for the design and evaluation of thin adhesive bonding in practical applications.

The material compressibility plays a crucial role in the delamination behavior in theory. We have discussed a parameter ϵ in Eq. (2.14) that can be used to characterize the effective compressibility of the thin adhesive layer, showing that it depends on both the intrinsic Poisson's ratio and the effective slenderness of the layer upon deflection. For thin layers with arbitrary compressibility, neither the perfectly compressible nor the perfectly incompressible model discussed in the literature is fully applicable. Instead, we have shown that a combined foundation model in Eq. (2.1), complemented by a generalized J -integral condition in Eq. (2.8), can provide a self-consistent description of this delamination problem. To solve the delamination problem for thin layers of arbitrary compressibility, a higher-order continuity condition is lacking and thus has to be informed by physical pictures. We found that it is more appropriate to use the continuity of pressure across the delamination front in planar peeling. However, the difference in the predicted delamination behavior caused by using the two different conditions is small when the delamination length exceeds a few thicknesses of the thin layer.

The compressibility parameter ϵ introduced in our work provides a rapid means of analyzing how soft substrate materials commonly used in MEMS and biomedical systems affect delamination behavior. The regime diagram based on the compressibility of the elastic layer and the lift-off height during peeling, allows readers to quickly identify the two most critical physical quantities in the delamination process—the detachment length and the peeling force. In practical experiments involving thin adhesive layers, achieving the highly incompressible regime $\epsilon \ll 1$ is generally difficult. Consequently, the difference between using the continuity of pressure or pressure gradient becomes negligible in highly compressible systems where $\epsilon \gg 1$.

Finally, we would like to emphasize that the relatively simple linear 1D model used in this work have enabled the exploration of some previously unclear features of the adhesive bonding problem. However,

we acknowledge that several important aspects have been overlooked. For example, the delamination front could become unstable and exhibit wavy-like patterns or interfacial cavitation in experiments [36,65,66], rendering our conclusion invalid. The experiments we focused on involve PDMS adhesives with relatively low adhesion energy, whereas high adhesion could induce both geometrical and material nonlinearities during the peeling that are not considered here [41,67]. We have focused on quasi-static peeling; however, in dynamic peeling scenarios, the rate dependence of adhesive layers becomes significant, leading to pronounced effects on interfacial strength [68–70]. This rate dependence is often characterized through empirical modifications of adhesion energy or by employing viscoelastic constitutive models to describe the adhesive layer's response during delamination [71–74]. However, these approaches introduce additional complexity to the theoretical description of interfacial failure. We have discussed a bending-dominated 1D case, while in the axisymmetric configuration, membrane stretching effects would become important as the peeling proceeds [75–78], which, along with potential wrinkling instabilities or buckling-driven delamination [79–81]. These limitations point to further investigations incorporating nonlinearities, dynamic effects, and instabilities to better understand the complex nature of adhesive bonding in various nature and engineering systems.

CRediT authorship contribution statement

Hang Li: Writing – original draft, Visualization, Investigation, Formal analysis. **Zhaohao Dai:** Writing – review & editing, Validation, Formal analysis, Conceptualization.

Declaration of competing interest

The authors declare that they have no known competing financial interests or personal relationships that could have appeared to influence the work reported in this paper.

Acknowledgments

We are grateful to Prof. Yueguang Wei for his inspiring mentorship. We also take this opportunity to warmly congratulate him on his 65th birthday and wish him continued happiness and success. This work was financially supported by the National Natural Science Foundation of China (Grant Nos. 12372103, 12302076, and 12432003). The authors thank Sheng Mao for useful discussions.

Appendix A. 1D solution for zero pressure

We used the boundary conditions in Eq. (2.18) and continuity conditions in Eq. (2.18) to obtain the constants in Eq. (2.24) in the main text. Specifically, we have the equation in Box I to be, where $g(\lambda_1, A, \theta, L)$ has been provided in Eq. (2.26).

Appendix B. 1D solution for zero pressure gradient

Under the assumption of a zero pressure gradient at the delamination front, we can still obtain the solution in the form of Eq. (2.24), but the detailed constants are given by the equation in Box II to be, where λ_1 , θ , and A are functions of ϵ identical to those in the main text while the function g reads

$$\begin{aligned} g(\lambda_1, A, \theta, L) = & 2A^3 \left[3 - 6 \cos \theta + \lambda_1 L \left((\lambda_1 L + 3)^2 - 6 \cos \theta (\lambda_1 L + 2) \right) \right] \\ & + 12 \lambda_1 A^2 (\lambda_1 L + 1) (\lambda_1 L + 1 - 2 \cos \theta) \sin \frac{\theta}{2} \\ & + 12 \lambda_1^2 A (1 - \cos \theta) (\lambda_1 L + 1) + 12 \lambda_1^3 \sin \frac{\theta}{2} \\ & + 4 A^4 L (\lambda_1^2 L^2 + 3 \lambda_1 L + 3) \sin \frac{\theta}{2}. \end{aligned} \quad (\text{B.2})$$

$$\begin{aligned}
C_1 &= \frac{\lambda_1^2 A^3}{2g(\lambda_1, A, \theta, L)}, \\
C_2 &= \frac{3 \lambda_1 A \left[-2 \lambda_1 - 4 \sin \frac{\theta}{2} (1 + \lambda_1 L) A - L (2 + \lambda_1 L) \lambda_1^2 \right]}{2g(\lambda_1, A, \theta, L)}, \\
C_3 &= \frac{3 e^{\lambda_1 L} A^4 (2 \sin \frac{\theta}{2} + L A)}{g(\lambda_1, A, \theta, L) (\lambda_1^2 - 2 \lambda_1 A \sin \frac{\theta}{2} + A^2)}, \\
C_4 &= \frac{\lambda_1^2 \sin \left(\theta + \Lambda L \cos \frac{\theta}{2} \right) - L \cos \left(\frac{3\theta}{2} + \Lambda L \cos \frac{\theta}{2} \right) \lambda_1^2 A + (1 + \lambda_1 L) A^2 \sin \left(2\theta + \Lambda L \cos \frac{\theta}{2} \right)}{g(\lambda_1, A, \theta, L) (\lambda_1^2 - 2 \lambda_1 A \sin \frac{\theta}{2} + A^2) / (3 e^{\Lambda L \sin \frac{\theta}{2}} \sec \frac{\theta}{2} \lambda_1^2)}, \\
C_5 &= \frac{\lambda_1^2 \cos \left(\theta + \Lambda L \cos \frac{\theta}{2} \right) + L \sin \left(\frac{3\theta}{2} + \Lambda L \cos \frac{\theta}{2} \right) \lambda_1^2 A + A^2 (1 + \lambda_1 L) \cos \left(2\theta + \Lambda L \cos \frac{\theta}{2} \right)}{-g(\lambda_1, A, \theta, L) (\lambda_1^2 - 2 \lambda_1 A \sin \frac{\theta}{2} + A^2) / (3 \lambda_1^2 e^{\Lambda L \sin \frac{\theta}{2}} \sec \frac{\theta}{2})},
\end{aligned} \tag{A.1}$$

Box I.

$$\begin{aligned}
C_1 &= \frac{\lambda_1^3 A^3 + 2 \lambda_1^2 A^4 \sin \frac{\theta}{2}}{g(\lambda_1, A, \theta, L)}, \\
C_2 &= \frac{\Lambda^2 [4 \cos \theta + \lambda_1 L (4 \cos \theta - \lambda_1 L - 4) - 2] - 2 \lambda_1^2 - [2 \Lambda^3 L (\lambda_1 L + 2) + 4 \lambda_1 A (\lambda_1 L + 1)] \sin \frac{\theta}{2}}{g(\lambda_1, A, \theta, L) / (3 \lambda_1 A)}, \\
C_3 &= \frac{6 \Lambda^5 e^{\lambda_1 L} (2 \Lambda L \sin \frac{\theta}{2} + 1 - 2 \cos \theta)}{g(\lambda_1, A, \theta, L) (\lambda_1^2 - 2 \lambda_1 A \sin \frac{\theta}{2} + A^2)}, \\
C_4 &= \frac{\lambda_1^3 \sin \left(\theta + \Lambda L \cos \frac{\theta}{2} \right) - \lambda_1^3 \Lambda L \cos \left(\frac{3\theta}{2} + \Lambda L \cos \frac{\theta}{2} \right) - \Lambda^3 (\lambda_1 L + 1) \cos \left(\frac{5\theta}{2} + \Lambda L \cos \frac{\theta}{2} \right)}{g(\lambda_1, A, \theta, L) (\lambda_1^2 - 2 \lambda_1 A \sin \frac{\theta}{2} + A^2) / (6 \lambda_1^2 \sec \frac{\theta}{2} e^{\Lambda L \sin \frac{\theta}{2}})}, \\
C_5 &= \frac{\lambda_1^3 \cos \left(\theta + \Lambda L \cos \frac{\theta}{2} \right) + \lambda_1^3 \Lambda L \sin \left(\frac{3\theta}{2} + \Lambda L \cos \frac{\theta}{2} \right) + \Lambda^3 (\lambda_1 L + 1) \sin \left(\frac{5\theta}{2} + \Lambda L \cos \frac{\theta}{2} \right)}{-g(\lambda_1, A, \theta, L) (\lambda_1^2 - 2 \lambda_1 A \sin \frac{\theta}{2} + A^2) / (6 \lambda_1^2 \sec \frac{\theta}{2} e^{\Lambda L \sin \frac{\theta}{2}})},
\end{aligned} \tag{B.1}$$

Box II.

$$F(L=0) = \frac{\lambda_1^2 A^2 (\lambda_1 + 2 \Lambda \sin \frac{\theta}{2})}{2 \lambda_1^3 \sin \frac{\theta}{2} + 4 \lambda_1^2 A \sin^2 \frac{\theta}{2} - 2 \lambda_1 A^2 (\sin \frac{3\theta}{2} - 2 \sin \frac{\theta}{2}) + \Lambda^3 (1 - 2 \cos \theta)} \cdot \frac{1}{F^{3/4}}. \tag{B.5}$$

Box III.

In this case, the condition to determine the delamination length becomes

$$\begin{aligned}
\Gamma &= \left[4 \lambda_1^3 \sin \frac{\theta}{2} - 2 \lambda_1^2 A (2 \lambda_1 L \cos \theta - \lambda_1 L - 4 \sin^2 \frac{\theta}{2}) \right. \\
&\quad \left. - 4 \lambda_1 A^2 \left(\sin \frac{3\theta}{2} - 2 \sin \frac{\theta}{2} \right) (1 + \lambda_1 L) \right. \\
&\quad \left. - 2 \Lambda^3 (2 \cos \theta - 1 - 4 \lambda_1 L \sin^2 \frac{\theta}{2}) - 2 \Lambda^4 (\lambda_1^3 - 2 L) \sin \frac{\theta}{2} - \lambda_1^2 A^5 (1 + \lambda_1 L) \right] \\
&\quad / \left[9 \lambda_1^2 A^4 g^2 (2 \lambda_1 \Lambda L + 2 \Lambda + 4 \lambda_1 \sin \frac{\theta}{2}) \right].
\end{aligned} \tag{B.3}$$

The peeling force is calculated by

$$F(L > 0) = \frac{6 \lambda_1^3 A^3 + 12 \lambda_1^2 A^4 \sin \frac{\theta}{2}}{g(\lambda_1, A, \theta, L) \Gamma^{3/4}}. \tag{B.4}$$

when delamination has occurred and by equation in Box III to be, if the interface does not delaminate yet.

Appendix C. Cohesive zone modeling

The simulation is performed using the commercial finite element software ABAQUS/Standard. Plane strain elements with 4-point integration are used for both the plate and the substrate. The geometry of the plate and substrate is modeled with dimensions of $10 \times 0.1 \text{ mm}^2$ and $10 \times 0.5 \text{ mm}^2$, respectively. The plate is treated as an isotropic elastic material with an elastic modulus of 10^4 MPa , while the substrate is modeled as a neo-Hookean material with a shear modulus of 0.5 MPa . The cohesive contact interaction is used to initially bond the plate and substrate. A typical bilinear cohesive law is applied in the finite element simulation, with a normal peak traction of T_c and a slope of K .

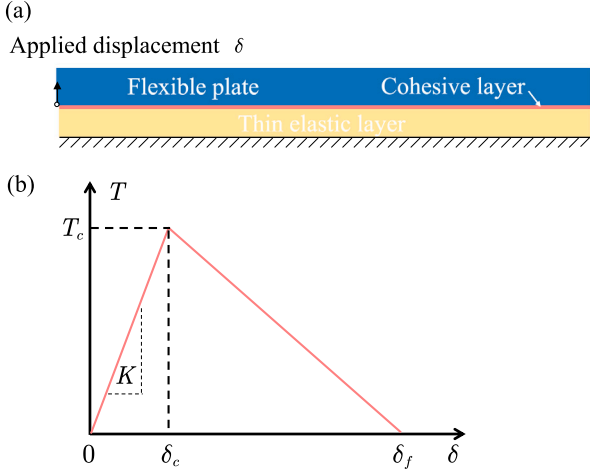


Fig. C.8. Cohesive zone modeling. (a) Schematic illustration of the model in finite element simulations. (b) The bilinear traction-separation law used to characterize the delamination at the interface.

In our theoretical model, interfacial failure is characterized solely by the interface energy, which is set to $\gamma = 40 \text{ mJ/m}^2$, as reported in the experimental work in Ref. [14]. In finite element simulations, however, the parameters T_c and K play a role in determining the early-stage peeling behavior. The bilinear traction-separation relation typically consists of two distinct stages: an initial separation stage followed by a damage evolution stage, which models interface failure.

To maintain consistency with our theoretical assumptions, we assume that the interface rapidly transitions to the damage evolution stage. This assumption requires the critical displacement δ_c to be sufficiently small and the stiffness K to be sufficiently large. Furthermore, the substrate is assumed to experience only small deformations, with a shear modulus set to 0.5 MPa. As a result, the maximum value of T_c is on the order of 0.01 MPa. With these considerations, we set $T_c = 0.01 \text{ MPa}$ and $K = 10^4 \text{ MPa/mm}$, which can ensure convergent simulation results at moderate delamination lengths. The maximum nominal stress criterion is employed to describe damage initiation, while an energy-based evolution model is used to represent the damage process. A vertical displacement δ is applied at the left end of the plate, and varying lifted heights at the left end of the plate are used to achieve different delamination lengths (see Fig. C.8).

Appendix D. Zero pressure or zero pressure gradient?

We have discussed the differences caused by the two distinct continuity conditions in the nearly compressible and incompressible regimes in the main text. In this appendix, we examine their differences for various values of ϵ . In the absence of the J -integral condition proposed in Eq. (2.8), previous work often adopts an energetic approach to determine the position of delamination at the perfectly incompressible limit [14,36]. We then compare the two approaches for thin layers with arbitrary compressibilities here. We then write the non-dimensionalized total free energy of the system as:

$$\bar{\Pi}[W(X), L] = \int_0^L \frac{1}{2} (W''')^2 dX + \int_L^\infty \frac{1}{2} (W''')^2 dX + \int_L^\infty \frac{1}{2} P W dX - \Gamma L, \quad (\text{D.1})$$

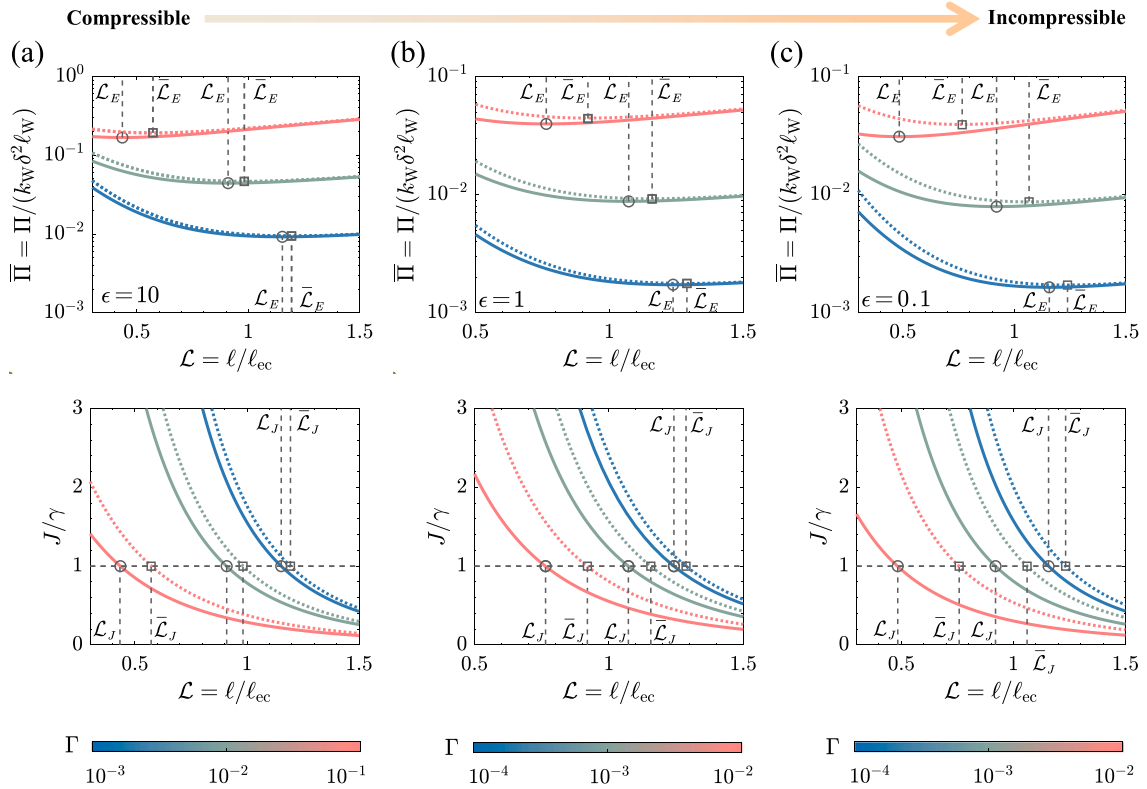


Fig. D.9. A comparison of J -integral approach and energy approach. The top panel shows the total free energy of the system as a function of the prescribed delamination lengths for thin layers with various effective adhesion energies and with $\epsilon = 10$ (a), $\epsilon = 1$ (b), and $\epsilon = 0.1$ (c). The bottom panel shows corresponding J by plugging the results in Eq. (2.8). All solid curves represent results obtained by enforcing the continuity of pressure at the delamination front (i.e., $p(\ell) = 0$), while the dotted curves correspond to results obtained by assuming the pressure force at the delamination front reaches its maximum (i.e., $p'(\ell) = 0$). In the top panel, \mathcal{L}_E and \mathcal{L}_E' denote the delamination lengths determined via the minimization of the total free energy calculated with $p(\ell) = 0$ and $p'(\ell) = 0$, respectively. In the bottom panel, \mathcal{L}_J and \mathcal{L}_J' denote the delamination lengths determined via $J = \gamma$, calculated with $p(\ell) = 0$ and $p'(\ell) = 0$, respectively.

where $\bar{\Pi} = \Pi/(k_w \delta^2 \ell_w)$ and Π is the dimensional total free energy. Given Γ and ϵ , we can use the boundary and continuity conditions to solve for $W(X)$ for different prescribed L . The true value of L is determined such that $\bar{\Pi}$ is minimized, as shown in the top panel of Fig. D.9. Note that all solid curves are solved with the continuity of pressure at $X = L$, while all dotted curves are solved with the continuity of the pressure gradient at $X = L$. In the bottom panel of Fig. D.9, we plot the value of J defined in Eq. (2.8) as a function of the prescribed L at given parameters (Γ, ϵ) .

As shown in the top panel of Fig. D.9, we denote the delamination length determined by $\partial \bar{\Pi} / \partial L = 0$ by \mathcal{L}_E (which uses the zero pressure condition) and $\bar{\mathcal{L}}_E$ (which uses the zero pressure gradient condition). In the bottom panel of Fig. D.9, we denote the delamination length determined by $J = \gamma$ by \mathcal{L}_J (which uses the zero pressure condition) and $\bar{\mathcal{L}}_J$ (which uses the zero pressure gradient condition). The results show that

$$\mathcal{L}_E(\Gamma, \epsilon) = \mathcal{L}_J(\Gamma, \epsilon) \quad \text{and} \quad \bar{\mathcal{L}}_E(\Gamma, \epsilon) = \bar{\mathcal{L}}_J(\Gamma, \epsilon) \quad (\text{D.2})$$

for various effective adhesion energies and compressibilities. This suggests the equivalence of the J -integral approach and the previously used energy approach. Notably, the J -integral approach can provide direct jump conditions, as discussed in the main text, allowing for immediate and even analytical solutions to the problem of arbitrary compressibilities without the need for tedious energy minimizing processes. Another observation from Fig. D.9 is that the difference between \mathcal{L} obtained using the zero pressure condition and $\bar{\mathcal{L}}$ obtained using the zero pressure gradient condition is rather quantitative for various ϵ , particularly at small Γ . This agrees with our findings in Figs. 5 and 6 in the main text.

Data availability

Data will be made available on request.

References

- [1] Wang W, Wei Z, Li YJ, You J, Li X, He J, et al. Multifunctional complementary field-effect transistors based on MoS₂/SWNTs heterostructures. *Appl Phys Lett* 2025;126(2).
- [2] Yu C, Zeng W, Wang B, Cui X, Gao Z, Yin J, et al. Stiffer is stickier: Adhesion in elastic nanofilms. *Nano Lett* 2025;25(5):1876–82.
- [3] Palmić TB, Slavić J. Design principles for a single-process 3D-printed stacked dielectric actuators—Theory and experiment. *Int J Mech Sci* 2023;246:108128.
- [4] Jin Z, Liu K, Pan E, Zhang Z, Lin C-P, Liu S. Spherical indentation over multilayered transversely isotropic media with imperfect interfaces. *Int J Mech Sci* 2024;109902.
- [5] Pei X, Yang W. Mixed elastohydrodynamic lubrication of transversely isotropic coatings in impact motion. *Int J Mech Sci* 2025;109944.
- [6] Dillard DA. *Advances in structural adhesive bonding*. Elsevier; 2023.
- [7] Cheng Y, Peng Z, Chen S. A theoretical model of enhanced adhesion of bioinspired micropillar arrayed surfaces. *J Mech Phys Solids* 2024;186:105592.
- [8] Liu J, Lin S, Liu X, Qin Z, Yang Y, Zang J, et al. Fatigue-resistant adhesion of hydrogels. *Nat Commun* 2020;11(1):1071.
- [9] Yuk H, Zhang T, Lin S, Parada GA, Zhao X. Tough bonding of hydrogels to diverse non-porous surfaces. *Nat Mater* 2016;15(2):190–6.
- [10] Yacobi B, Martin S, Davis K, Hudson A, Hubert M. Adhesive bonding in microelectronics and photonics. *J Appl Phys* 2002;91(10):6227–62.
- [11] Bartlett MD, Case SW, Kinloch AJ, Dillard DA. Peel tests for quantifying adhesion and toughness: A review. *Prog Mater Sci* 2023;137:101086.
- [12] Xiang Y, Hwang D, Wan G, Niu Z, Ellison CJ, Francis LF, et al. Mechanics of peeling adhesives from soft substrates: A review. *J Appl Mech* 2025;92(2):020801.
- [13] Kaelble DH. Peel adhesion: micro-fracture mechanics of interfacial unbonding of polymers. *Trans Soc Rheol* 1965;9(2):135–63.
- [14] Ghatak A, Mahadevan L, Chaudhury MK. Measuring the work of adhesion between a soft confined film and a flexible plate. *Langmuir* 2005;21(4):1277–81.
- [15] Barber JR. In: *Contact mechanics*, vol. 20, Springer; 2018.
- [16] Hao S, Huang R, Rodin GJ. Approximate analytical solutions for the energy release rate of planar cracks in constrained elastic thin layers. *Int J Fract* 2025;250(1):1–23.
- [17] Cricri G, Perrella M. A fracture toughness identification method for the debonding test of DCB specimens accounting for three-dimensional effects. *Int J Solids Struct* 2025;113350.
- [18] Long H, Liu Y, Yin H, Zhang Y, Yang Q, Wei Y. 90-Degree peeling of elastic thin films from elastic soft substrates: Theoretical solutions and experimental verification. *J Mech Phys Solids* 2024;193:105855.
- [19] Dillard DA, Mukherjee B, Karnal P, Batra RC, Frechette J. A review of Winkler's foundation and its profound influence on adhesion and soft matter applications. *Soft Matter* 2018;14(19):3669–83.
- [20] Skotheim J, Mahadevan L. Soft lubrication. *Phys Rev Lett* 2004;92(24):245509.
- [21] Yang F. Asymptotic solution to axisymmetric indentation of a compressible elastic thin film. *Thin Solid Films* 2006;515(4):2274–83.
- [22] Zhang Y, Zhao Y. A precise model for the shape of an adhered microcantilever. *Sens Actuators A* 2011;171(2):381–90.
- [23] Argatov I, Mishuris G, Popov V. Asymptotic modelling of the JKR adhesion contact for a thin elastic layer. *Q J Mech Appl Math* 2016;69(2):161–79.
- [24] Plaut RH, Hwang D, Lee C, Bartlett MD, Dillard DA. Peeling of finite-length elastica on Winkler foundation until complete detachment. *Int J Solids Struct* 2022;256:111944.
- [25] Li H, Dai Z. Adhesion of elastic microbeams on thin deformable substrates. *Eng Fract Mech* 2024;110634.
- [26] Dillard DA. Bending of plates on thin elastomeric foundations. *J Appl Mech* 1989;56(2):382–6.
- [27] Chandler TG, Vella D. Validity of Winkler's mattress model for thin elastomeric layers: Beyond Poisson's ratio. *Proc R Soc A* 2020;476(2242):20200551.
- [28] Ghatak A, Chaudhury MK. Adhesion-induced instability patterns in thin confined elastic film. *Langmuir* 2003;19(7):2621–31.
- [29] Mukherjee B, Dillard DA. On buckling of a thin plate on an elastomeric foundation. *Int J Mech Sci* 2018;149:429–35.
- [30] Dai Z, Vella D. Droplets on lubricated surfaces: The slow dynamics of skirt formation. *Phys Rev Fluids* 2022;7(5):054003.
- [31] Bertin V, Amarouchene Y, Raphaël E, Salez T. Soft-lubrication interactions between a rigid sphere and an elastic wall. *J Fluid Mech* 2022;933:A23.
- [32] Rallabandi B. Fluid-elastic interactions near contact at low Reynolds number. *Annu Rev Fluid Mech* 2024;56(1):491–519.
- [33] Plaut RH, Dillard DA. Peeling of finite-length plates from an elastomeric foundation: A 1D cylindrical bending solution. *J Appl Mech* 2023;90(9):091001.
- [34] Yang F. Adhesive contact between a rigid axisymmetric indenter and an incompressible elastic thin film. *J Phys D: Appl Phys* 2002;35(20):2614.
- [35] Ghatak A, Mahadevan L, Chung JY, Chaudhury MK, Shenoy V. Peeling from a biomimetically patterned thin elastic film. *Proc R Soc A* 2004;460(2049):2725–35.
- [36] Ghatak A. Peeling off an adhesive layer with spatially varying modulus. *Phys Rev E* (3) 2010;81(2):021603.
- [37] Mukherjee B, Batra RC, Dillard DA. Effect of confinement and interfacial adhesion on peeling of a flexible plate from an elastomeric layer. *Int J Solids Struct* 2017;110:385–403.
- [38] Chadwick RS. Axisymmetric indentation of a thin incompressible elastic layer. *SIAM J Appl Math* 2002;62(5):1520–30.
- [39] Adda-Bedia M, Mahadevan L. Crack-front instability in a confined elastic film. *Proc R Soc A* 2006;462(2075):3233–51.
- [40] Dogru S, Aksoy B, Bayraktar H, Alaca BE. Poisson's ratio of PDMS thin films. *Polym Test* 2018;69:375–84.
- [41] Hao S, Huang R, Rodin GJ. Constitutive models for confined elastomeric layers: Effects of nonlinearity and compressibility. *Mech Mater* 2024;190:104912.
- [42] Im SH, Huang R. Evolution of wrinkles in elastic-viscoelastic bilayer thin films. *J Appl Mech* 2005;72(6):955–61.
- [43] Movchan AB, Rebrow KR, Rodin GJ. Axisymmetric deformation of compressible, nearly incompressible, and incompressible thin layers between two rigid surfaces. *Int J Solids Struct* 2021;214:61–73.
- [44] Yu C, Dai Z. Premature jump-to-contact with elastic surfaces. *J Mech Phys Solids* 2024;193:105919.
- [45] Argatov I, Mishuris G, Argatov I, Mishuris G. Deformation of a thin bonded transversely isotropic elastic layer. *Contact Mech Articul Cartil Layers: Asymptot Model* 2015;1–18.
- [46] Li J, Zhang G, Wang L, Dai Z. Indentation of a plate on a thin transversely isotropic elastic layer. *Acta Mech Solida Sin* 2024;1–10.
- [47] Mansfield EH. *The bending and stretching of plates*. Cambridge University Press; 1989.
- [48] Glassmaker N, Hui C. Elastica solution for a nanotube formed by self-adhesion of a folded thin film. *J Appl Phys* 2004;96(6):3429–34.
- [49] Majidi C. Remarks on formulating an adhesion problem using Euler's elastica (draft). *Mech Res Commun* 2007;34(1):85–90.
- [50] Majidi C, Adams GG. A simplified formulation of adhesion problems with elastic plates. *Proc R Soc A* 2009;465(2107):2217–30.
- [51] Bico J, Reyssat É, Roman B. Elastocapillarity: When surface tension deforms elastic solids. *Annu Rev Fluid Mech* 2018;50:629–59.
- [52] Li H, Yu C, Dai Z. Regimes in the axisymmetric stiction of thin elastic plates. *Int J Mech Sci* 2024;284:109740.

- [53] Rice JR. A path independent integral and the approximate analysis of strain concentration by notches and cracks. *J Appl Mech* 1968;35(2):379–86.
- [54] Hutchinson JW, Suo Z. Mixed mode cracking in layered materials. *Adv Appl Mech* 1991;29:63–191.
- [55] Yuan Z, Kardomateas GA. High-order theory approach for debonded sandwich panels—Part II: Energy release rate and mode mixity. *J Appl Mech* 2025;92(2).
- [56] Chen E, Dai Z. Elastic sheets on Winkler foundations: Indentation stiffness and nonlinearities. *Int J Solids Struct* 2025;113346.
- [57] Wang X, Chen E, Wu Q, Yuan X, Zhang T, Zhu S, et al. Probing the elastic coupling at Van der Waals interfaces of two-dimensional materials. *Phys Rev B* 2025;111(12):125418.
- [58] Na SR, Suk JW, Tao L, Akinwande D, Ruoff RS, Huang R, et al. Selective mechanical transfer of graphene from seed copper foil using rate effects. *ACS Nano* 2015;9(2):1325–35.
- [59] Dai Z, Lu N, Liechti KM, Huang R. Mechanics at the interfaces of 2D materials: Challenges and opportunities. *Curr Opin Solid State Mater Sci* 2020;24(4):100837.
- [60] Obreimoff J. The splitting strength of mica. *Proc R Soc A* 1930;127(805):290–7.
- [61] Mukherjee B, Batra RC, Dillard DA. Edge debonding in peeling of a thin flexible plate from an elastomer layer: A cohesive zone model analysis. *J Appl Mech* 2017;84(2):021003.
- [62] Long H, Liu Y, Yin H, Wei Y. Influence of the shape of cohesive zone models on the peeling of stiff film/soft substrate systems: A theoretical perspective. *Mech Mater* 2025;105343.
- [63] Peng Z, Chen S. Effect of bending stiffness on the peeling behavior of an elastic thin film on a rigid substrate. *Phys Rev E* 2015;91(4):042401.
- [64] Barber J, Stupkiewicz S. Indentation of a thin incompressible layer with finite friction. *Int J Solids Struct* 2024;298:112868.
- [65] Juel A, Pihler-Puzović D, Heil M. Instabilities in blistering. *Annu Rev Fluid Mech* 2018;50(1):691–714.
- [66] Shen J, He Z, Chen H, Yang Y, Jiang H. Exploiting interfacial instability during peeling a flexible plate from elastic films. *J Mech Phys Solids* 2024;192:105821.
- [67] Zhou Z, Jia Y, Lu W, Lei J, Liu Z. Enhancing the crack initiation resistance of hydrogels through crosswise cutting. *J Mech Phys Solids* 2024;183:105516.
- [68] Tricarico M, Ciavarella M, Papangelo A. Enhancement of adhesion strength through microvibrations: Modeling and experiments. *J Mech Phys Solids* 2025;106020.
- [69] Papangelo A, Ciavarella M. Detachment of a rigid flat punch from a viscoelastic material. *Tribol Lett* 2023;71(2):48.
- [70] Mandriota C, Menga N, Carbone G. Enhancement of adhesion strength in viscoelastic unsteady contacts. *J Mech Phys Solids* 2024;192:105826.
- [71] Yin H, Ma Y, Feng X. Rate-dependent peeling behavior of the viscoelastic film-substrate system. *Int J Solids Struct* 2024;286:112588.
- [72] Wang Z, Liu X. Pull-off of viscoelastic spherical contact. *J Adhes Sci Technol* 2024;38(16):2989–3007.
- [73] Ciavarella M. Improved muller approximate solution of the pull-off of a sphere from a viscoelastic substrate. *J Adhes Sci Technol* 2021;35(20):2175–83.
- [74] Wang Q, Papangelo A, Ciavarella M, Gao H, Li Q. Rapid detachment of a rigid sphere adhered to a viscoelastic substrate: An upper bound model incorporating Maugis parameter and preload effects. *J Mech Phys Solids* 2025;106028.
- [75] Fang Z, Dai Z, Wang B, Tian Z, Yu C, Chen Q, et al. Pull-to-peel of two-dimensional materials for the simultaneous determination of elasticity and adhesion. *Nano Lett* 2022;23(2):742–9.
- [76] Chen E, Dai Z. Axisymmetric peeling of thin elastic films: A perturbation solution. *J Appl Mech* 2023;90(10):101011.
- [77] Dai Z. Analytical solutions for circular elastic membranes under pressure. *J Appl Mech* 2024;91(8):081002.
- [78] Li K, Han Z, Liang H. Weakened adhesion on elastic film via patterned adhesion. *Int J Mech Sci* 2025;109992.
- [79] Dai Z, Sanchez DA, Brennan CJ, Lu N. Radial buckle delamination around 2D material tents. *J Mech Phys Solids* 2020;137:103843.
- [80] Box F, Domino L, Corvo TO, Adda-Bedia M, Démary V, Vella D, et al. Delamination from an adhesive sphere: Curvature-induced dewetting versus buckling. *Proc Natl Acad Sci USA* 2023;120(12):e2212290120.
- [81] Liu S, He J, Rao Y, Dai Z, Ye H, Tanir JC, et al. Conformability of flexible sheets on spherical surfaces. *Sci Adv* 2023;9(16):eadf2709.